Early Oxidation Processes on the Greigite Fe₃S₄(001) Surface by Water: A Density Functional Theory Study

David Santos-Carballal,*,†,‡ Alberto Roldan,† and Nora H. de Leeuw*,†,‡,§

†School of Chemistry, Cardiff University, Main Building, Park Place, Cardiff CF10 3AT, U.K.
‡Department of Chemistry, University College London, 20 Gordon Street, London WC1H 0AJ, U.K.
§Department of Earth Sciences, Utrecht University, Princetonplein 9, 3584 CC Utrecht, The Netherlands

⑤ Supporting Information

ABSTRACT: Greigite (Fe_3S_4), the sulfide counterpart of the spinel-structured oxide material magnetite (Fe_3O_4), is a mineral widely identified in anoxic aquatic environments and certain soils, which can be oxidized, thereby producing extremely acid solutions of sulfur-rich wastewaters, so-called acid mine drainage (AMD) or acid rock drainage (ARD). Here we report a computational study of the partial replacement of sulfur (forming H_2S) by oxygen (from H_2O) in the $Fe_3S_4(001)$ surface, derived from density functional theory calculations with on-site Coulomb approach and long-range dispersion corrections (DFT+U−D2). We have proposed three pathways for the oxidation of the surface as a function of H_2O coverage and pH. Different pathways give different intermediates, some of which are followed by a solid-state diffusion of the O atom. Low levels of H_2O coverage, and especially basic conditions, seem to be essential, leading to the most favorable energetic landscape for the oxidation of the $Fe_3S_4(001)$ surface. We have derived the thermodynamic and kinetic profile for each mechanism and plotted the concentration of H_2S and protons in aqueous solution and thermodynamic equilibrium with the stoichiometric and partially oxidized $Fe_3S_4(001)$ surface as a function of the temperature. Changes in the calculated vibrational frequencies of the adsorbed intermediates are used as a means to characterize their transformation. We have taken into account statistical entropies for H_2S and H_2O and other experimental parameters, showing that this mineral may well be among those responsible for the generation of AMD.
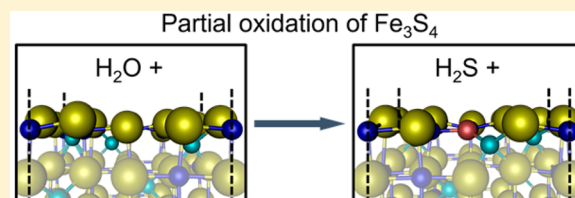
1. INTRODUCTION

Extremely acidic sulfur-rich wastewaters are a current worldwide problem. So-called acid mine drainage (AMD) or acid rock drainage (ARD) is associated with natural weathering of rock formations[1] but aggravated, in particular, by existing and historic human activities such as the mining industry.[2−4] Once mining or processing operations expose metal sulfide compounds, in particular pyrite (cubic FeS_2), to weathering elements such as O_2 and H_2O[5] as well as certain microorganisms,[6−8] the minerals steadily oxidize. This process results in reduction of the water pH[9] and potentially high concentrations of toxic metallic and metalloid elements in solution,[10] depending on the initial composition of the exposed minerals.

A number of chemical reactions leading to oxidation and dissolution of metal sulfides have been studied, and several mechanisms have been suggested, depending on the minerals and the oxidizing agent present. One of the most remarkable mechanisms, called the polysulfide mechanism, is characteristic of acid-soluble sulfides, such as sphalerite (ZnS), where protons attack the mineral and produce H_2S. Sulfur-oxidizing bacteria further oxidize the H_2S to $SO_4^{2−}$ regenerating the protons.[6] Thiosulfate, the other important mechanism characteristic of nonacid-soluble persulfides, such as FeS_2,[11] proceeds initially by an attack of aqueous Fe^{3+} ions to the metal sulfide mineral, thereby generating protons, thiosulfate ($S_2O_3^{2−}$) and Fe^{2+}. This

Fe^{2+} is then reoxidized by iron-oxidizing bacteria, while $S_2O_3^{2−}$ decomposes into elemental sulfur and $SO_4^{2−}$ ions.[6−8]

Iron sulfides are the predominant sulfides found in anoxic marine sediments[12] and therefore one of the main causes of AMD.[5,13,14] FeS_2 is a stable mineral in these environments[12,15,16] and considerable research effort has been devoted to study its oxidation,[7,8,17−23] but other usually coexisting iron sulfides have been largely overlooked. Among other minerals, the spinel-structured greigite (Fe_3S_4) is a metastable intermediate in the formation pathway of FeS_2 from mackinawite (tetragonal FeS),[24−28] which has a long environmental persistence[29] and can also be found in aquatic environments[30−35] and soils[36,37] as well as in magnetotactic bacteria[38] and gastropods.[39]

Fe_3S_4 solubility has been rationalized mostly as a digestion, ignoring other important oxidation processes that can take place in aqueous medium. It has been suggested that, during digestion, the mineral forms 0.75 parts of H_2S and disproportionates to Fe^{2+} and orthorhombic sulfur.[40] However, elemental sulfur was not formally identified even after exposing Fe_3S_4 to a mixture of mineral acids and reducing agents and was therefore assumed to be the sulfur content not recovered (25% of S in
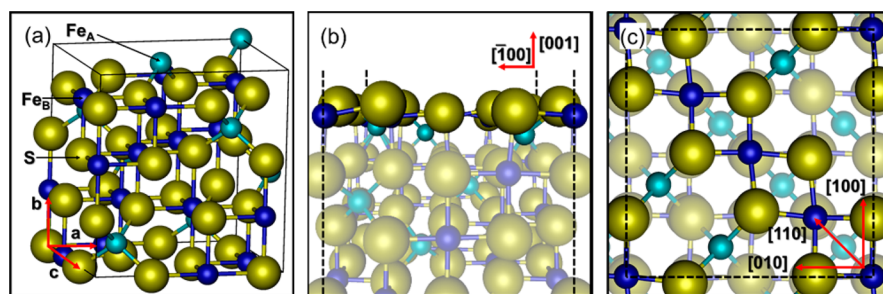
Figure 1. (a) Unit cell of Fe$_3$S$_4$ showing the cubic spinel crystal structure and the (b) side and (c) top views of its (001) surface. Fe$_A$ atoms are in light blue, Fe$_B$ atoms are in dark blue, and S atoms are in yellow. Layers with atoms with dangling bonds are highlighted in (b) and (c).

Fe$_3$S$_4$). In another study of the dissolution of Fe$_3$S$_4$ in distilled water under an H$_2$S atmosphere, orthorhombic sulfur was again considered as one of the products even though it was not detected.[41] This assumption was based on the fact that the oxidation potential of this process was close to that of the half-cell involving H$_2$S and elemental sulfur.

Purity of the samples is another issue affecting the accurate measurement of Fe$_3$S$_4$ solubility, which is usually difficult to control due to the unavoidable copresence of FeS and FeS$_2$. For example, less sulfur can be recovered from Fe$_3$S$_4$ aged for 1 week than from freshly prepared samples as it slowly oxidizes to pyrite, requiring harsher conditions to dissolve.[40] So far, due to the metastable nature of this mineral, any attempt to quantify Fe$_3$S$_4$ solubility has been difficult to reproduce, with highly uncertain and low sulfur recoveries.[42] The analysis of Fe$_3$S$_4$ in a mixture of iron sulfides has also been found to be inaccurate as the dissolution stoichiometry is difficult to control.[40,43−48] Moreover, the apparent value measured for Fe$_3$S$_4$ by Berner[41] could be artificially increased, since each iron sulfide phase present has a different solubility.[49]

Given the importance of Fe$_3$S$_4$ as a contributor in the formation of AMD and the experimental inaccuracies in the determination of its solubility, in this paper we present a fresh description of the early oxidation stages of this mineral. Taking into account the structural differences between FeS$_2$ and Fe$_3$S$_4$ and the decisive role of the persulfide group in dictating the mechanism of the oxidation reactions of metal sulfides,[6] we have used density functional theory (DFT) calculations to investigate the early oxidation processes of Fe$_3$S$_4$ via a polysulfide mechanism, in order to explain this mineral's lability in a disturbed aqueous medium. We propose three mechanisms to account for the partial replacement of S by O atom in the top layer of the Fe$_3$S$_4$(001) surface, which is the most prominent plane in solvothermal synthesized nano-particles.[50] We have provided the simulated infrared (IR) spectra of the intermediates along the oxidation mechanisms. We have also applied thermodynamic arguments to examine the pH conditions and the H$_2$S concentration, in aqueous solution and temperatures at which these species are in equilibrium with the stoichiometric and oxidized Fe$_3$S$_4$(001) surface, which is relevant to the geochemical formation of AMD.

2. COMPUTATIONAL METHODS

2.1. Calculation Details. We have performed spin-polarized calculations with the Vienna *ab initio* simulation package (VASP).[51−54] All simulations were carried out within the periodic plane-wave DFT framework. The projector augmented wave (PAW) method was used to describe the

core electrons and their interaction with the valence ones.[55,56] The frozen core of the Fe, S, and O elements was defined up to and including the 3p, 2p, and 1s electrons, respectively. At the level of the generalized gradient approximation (GGA), the exchange-correlation in the form of the Perdew−Wang 91 (PW91)[57,58] functional was used together with the spin interpolation of Vosko et al.[59] The long-range dispersion interactions were added via the semiempirical method of Grimme (D2),[60] using the global scaling factor parameter optimized for the Perdew−Burke−Ernzerhof (PBE)[61,62] functional, $s_6 = 0.75$, which has shown to provide good results in the modeling of a number of sulfides.[63−68] Brillouin zone integrations of the surface slabs were performed using a Γ-centered Monkhorst−Pack grid[69] of 4 × 4 × 1 k-points. The isolated H$_2$O and H$_2$S molecules were modeled in a cell with broken symmetry which was big enough to avoid intermo-lecular interactions, sampling only the Γ point of the Brillouin zone. In order to increase the integration efficiency in the reciprocal space, the partial occupancies for all calculations were determined using the tetrahedron method with Blöchl corrections.[70] Kohn−Sham (KS) valence states were expanded in a plane-wave basis set with the kinetic energy's cutoff fixed at 600 eV. The DFT + U[71] version of Dudarev et al.[72] was used for the description of the localized and strongly correlated d Fe electrons. On the basis of previous work, we have chosen a U_{eff} of 1.0 eV.[50,73−75] Electronic density optimization was stopped when the total energy difference between two consecutive self-consistent loop steps was below 10^{-5} eV. Atomic positions were relaxed to their ground state using the conjugate-gradient method and were considered converged when the Hellmann−Feynman forces on all atoms were smaller than 0.02 eV·Å^{-1}. The dimer method was used to search the transition states (TS),[76,77] which were characterized by a single imaginary frequency along the reaction coordinate. Higher cutoff values and k-point grids, as well as a lower self-consistent energy threshold, were tested to ensure energies were converged within 1 meV per atom.

Fe$_3$S$_4$ has a spinel crystal structure characterized by the space group $Fd\bar{3}m$.[35] The face-centered cubic unit cell is composed of 32 sulfur anions, which are almost regularly close packed along the [111] direction. This S arrangement generates 8 tetrahedral (A) and 16 octahedral (B) holes per unit cell occupied by Fe cations, see Figure 1, part a. Fe$_3$S$_4$ is a 2−3 type spinel, which classification is based on the cation oxidation state. This spinel has an inverse cation distribution Fe$_A$$^{3+}$[Fe^{2+}Fe^{3+}]$_BS_4$$^{2-}$, where half of the Fe^{3+} cations are filling the A positions and all the Fe^{2+} together with the rest of the Fe^{3+} ions are occupying the B holes.[78−82] Initial magnetic moments of the A and B sublattices

Table 1. Summary of the Calculated Wavenumbers for the Fundamental Vibrational Modes (Unscaled and Scaled) of the Isolated H_2O and H_2S Molecules in cm^{-1} along with the Experimental Values for the Gas Phase Molecules[a]

		H_2O			H_2S		
		ν_{asym}	ν_{sym}	δ	ν_{asym}	ν_{sym}	δ
calculated	unscaled	3886.2	3763.3	1587.9	2663.0	2650.9	1187.2
	scaled	3796.4	3676.3	1551.2	2601.5	2598.6	1159.8
experimental[99]		3756	3657	1595	2626	2615	1183

[a]The presented vibrational modes are the asymmetric stretching (ν_{asym}), symmetric stretching (ν_{sym}) and bending (δ) modes.
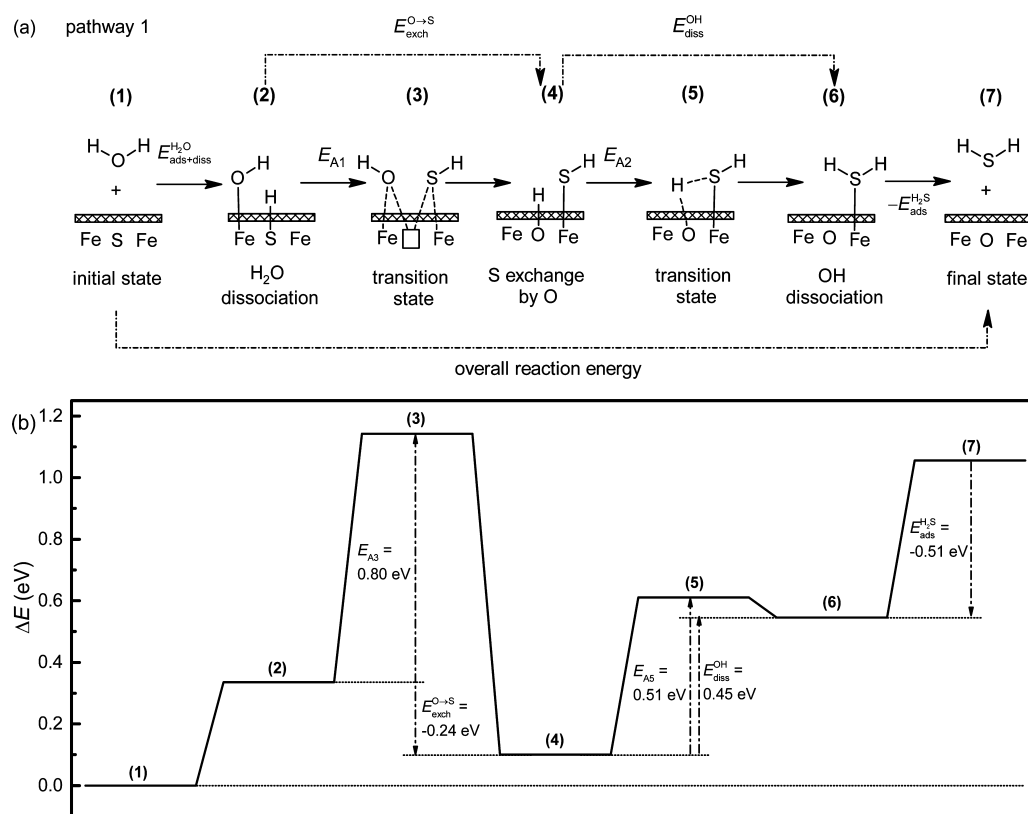

Figure 2. (a) Mechanism and (b) reaction profile for the oxidation of the $Fe_3S_4(001)$ surface via pathway 1.

were set antiparallel, with the Fe ions in high-spin states, in line with previous studies.[73,74]

2.2. Surface Models. Surface calculations were carried out using a symmetric and nondipolar stoichiometric slab.[83] This well-defined surface, which is only an approximate model of a real surface, is essential for calculating accurate and realistic surface properties.[84−88] The geometry optimized topmost layer of the (001) surface terminates in a bulk-like structure containing single rows in the [110] direction of 5-coordinated Fe_B ions alternating every two single rows of S ions with cubic packing, see Figure 1, parts b and c. Beneath this layer, there are 1.5 monolayers (ML) of 4-coordinated Fe_A also forming rows parallel to the S ones. From this layer, 0.5 ML of Fe_A with a $(\sqrt{2} \times \sqrt{2})R\,45°$ symmetry originates from above the surface, which moved inward during relaxation. The surface was modeled with a slab composed of 8 formula units of Fe_3S_4 and exposing a surface area of 93.53 $Å^2$. The slab model was formed by eight atomic layers, in which the five bottom-most layers were kept frozen at their relaxed bulk positions, while the remaining top layers were allowed to optimize. A vacuum of 12 Å was added between the periodic slabs in the direction perpendicular to the surface. Convergence of the slab energy

within 1 meV per atom was further tested with different slab and vacuum thickness as well as a number of relaxed layers. In order to enhance the electronic convergence, dipole corrections perpendicular to the surface were included in our simulations to account for any dipole created by the chemical species added in the relaxed surface of the slab.[89,90]

A Bader charge analysis was used to partition the electron density grid into atomic charges.[91−93] Charge density flow diagrams were constructed by subtracting from the electronic charge density of the total adsorbate−surface system, the sum of the charge densities of the isolated adsorbate and clean surface in the same geometry.

For further information, the optimized lattice (a) and sulfur parameters (u), the total magnetization of saturation (M_S), the atomic spin moments (m_s) and the atomic charges (q) of bulk Fe_3S_4 are shown in Table SI-1 (Supporting Information). The density of states of the bulk and (001) surface of Fe_3S_4 are also presented in Figure SI-1.

2.3. Simulation of the Infrared Spectra. Vibrational frequencies were determined for the isolated H_2O and H_2S molecules and for the reaction intermediates on the $Fe_3S_4(001)$ surface for each state of each mechanism. We have used central

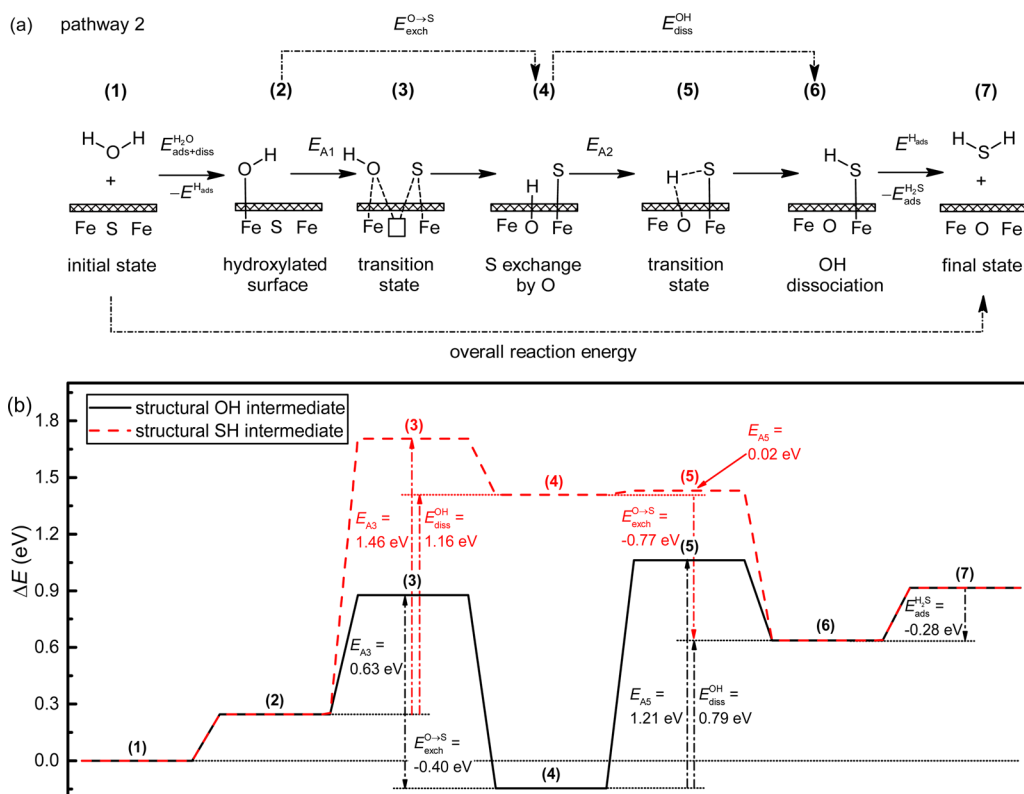**Figure 3.** (a) Mechanism and (b) reaction profile for the oxidation of the $Fe_3S_4(001)$ surface via pathway 2.

finite differences, by allowing each ion to move in the direction of each Cartesian coordinate by a small negative and positive displacement, to calculate the Hessian matrix. The prediction of the vibrational frequencies from the second derivative of the potential energy with respect to the atomic positions takes into account only the curvature at the minimum of the well. In this region of the energy surface, the potential has a harmonic behavior, meaning that the vibrational energy levels are equally spaced. In contrast, the fundamental modes observed experimentally usually correspond to the transition between the $\nu = 0$ and the $\nu = 1$ vibrational energy levels of an anharmonic potential energy surface. To compensate for the approximate nature of the calculated vibrational frequencies, they are usually corrected with an empirical scale factor.[94−98]

We have reported in Table 1 the calculated values for the fundamental vibrational modes (unscaled and scaled) of the isolated H_2O and H_2S molecules. The quality of the calculated quantities can be assessed through comparison with the experimental values for the gas phase molecules,[99] also shown in Table 1. The scaling factor is calculated as $c = \sum(\omega_{exp} \cdot \omega_{calc}^2)/\sum\omega_{calc}^2$, while its uncertainty is obtained from $u = (\sum(\omega_{calc}^2(c - \omega_{exp}/\omega_{calc})^2))/\sum\omega_{calc}^2$, where ω_{calc} and ω_{exp} are the calculated and experimentally observed IR wavenumbers, respectively.[94] The value of $c = 0.98 \pm 0.01$ for our set of two molecules indicates a good predictive behavior of the PW91 functional for vibrational frequencies. The largest difference between the unscaled (scaled) calculated wavenumbers and experiments is 130.2 (−43.8) cm^{-1} and the smallest is 4.2 (19.3) cm^{-1}, while the uncertainty of the largest unscaled wavenumber is 38.9 cm^{-1}. Taking into account that the PW91 functional provides sufficiently accurate IR frequencies, we are confident of our predicted vibrational wavenumbers for the adsorbed intermediates presented in this study.[94−98] In

subsequent sections, only the unscaled wavenumbers are presented.

We have only allowed the displacement of atoms with dangling bonds and adsorbed species for the simulation of the IR spectra. The coupling between the adsorbates and surface phonons, all of which appear below 400 cm^{-1}, was neglected. The intensities of the fundamental IR bands, the square root of the dynamic dipole moments, were determined by projecting the derivative of the dipole moment onto the basis of normal modes. Each vibrational band was smeared with a Gaussian function.

2.4. Thermodynamic and Kinetic Profiles. We have modeled three mechanisms for the initial stages of the $Fe_3S_4(001)$ surface oxidation at various H_2O coverage and pH regimes. Note that in our approximated model we have neglected the water environment and the zero point energy corrections. The relative energy of the system (ΔE_j) for every state j along the proposed thermodynamic and kinetic profile with respect to the energies of the pristine relaxed $Fe_3S_4(001)$ surface slab (E_{slab}) and an isolated H_2O molecule in vacuum (E_{H_2O}) was calculated according to the following equation,

$$\Delta E_j = E_{system} - nE_{H_2O} - E_{slab} \tag{1}$$

where n represents the number of H_2O molecules.

The adsorption energy (E_{ads}^i) of the species i is determined from the difference between ΔE_j of the adsorbed state j and the previous one $j - 1$. The dissociation energy (E_{diss}^i) is obtained from the difference between ΔE_j of the dissociated state j and the state $j - 2$. The activation energy (E_{Aj}) is calculated from the difference between ΔE_j of the transition state j and the intermediate of the state $j - 1$. The energy required to substitute one S atom or SH group in the mineral surface by an
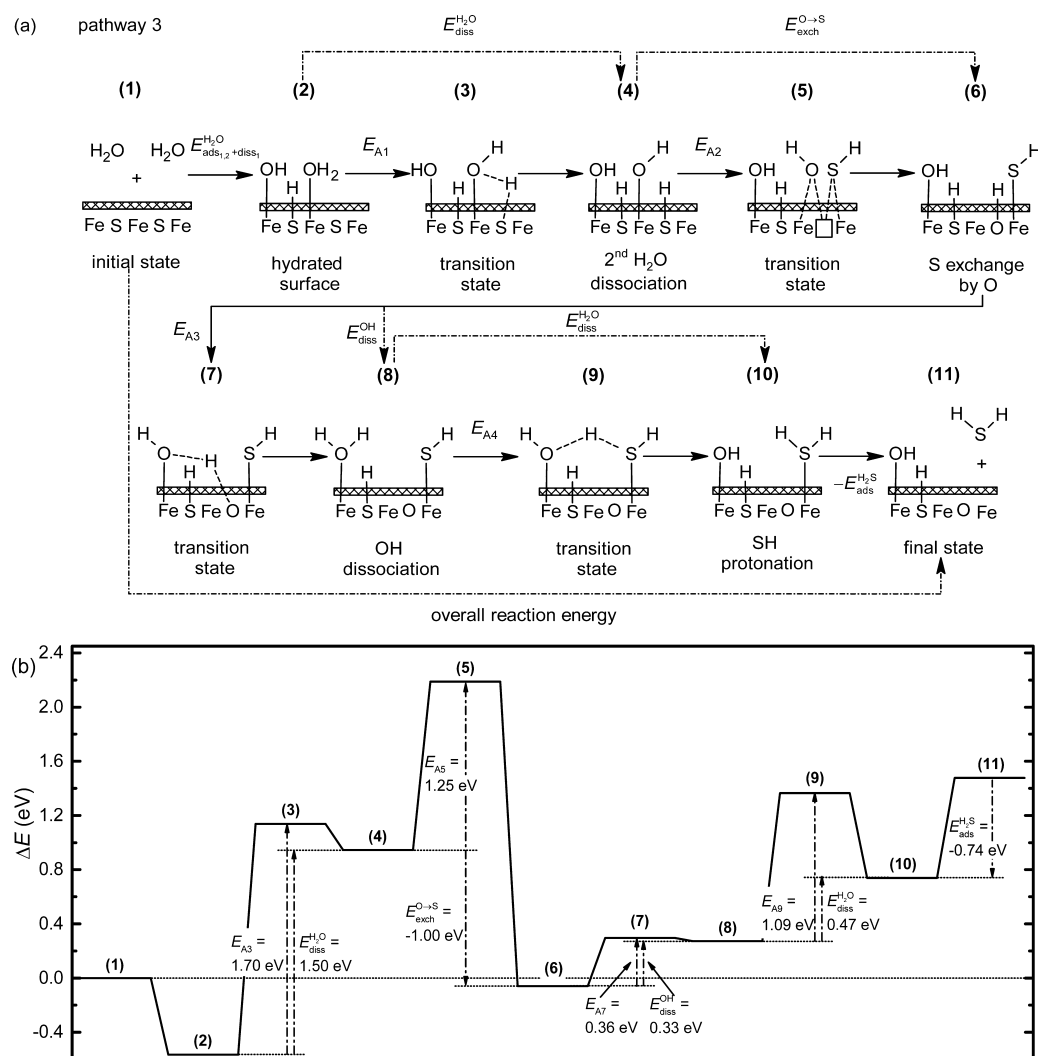
Figure 4. (a) Mechanism and (b) reaction profile for the oxidation of the $Fe_3S_4(001)$ surface via pathway 3.

adsorbed OH group ($E_{exch}^{O \rightarrow S}$) is derived from the difference between ΔE_j of the states after and before substitution.

3. RESULTS AND DISCUSSION

3.1. Oxidation of the $Fe_3S_4(001)$ Surface. We have considered three main mechanisms for studying the oxidation of the $Fe_3S_4(001)$ surface through the partial exchange of S from the top layer by O from the water producing H_2S, see Figure 2, part a, Figure 3, part a, and Figure 4, part a. For pathway 1 (2), we added 1 H_2O (OH) nm^{-2} of surface, whereas for pathway 3 the amount of H_2O was doubled.[100] Note that we have chosen the most favorable adsorption configuration of H_2O and OH as the initial states for the oxidation calculations.

3.1.1. Pathway 1. The dissociation of one H_2O molecule on the (001) surface is thermodynamically most favorable if its O atom coordinates an Fe_B ion at a distance of 1.83 Å; see state 2 in Figure 5. Although all Fe_B are equivalent in this surface, the existence of the Fe_A ions and the newly absorbed H_2O molecule generates four nonequivalent types of S ions around the hydroxylated Fe_B ion. The dissociated H lies between the S next to the hydroxylated Fe_B and at the tetrahedral cavity of the Fe_A row in the [110] direction. The charge analysis of state 2 indicates that, upon dissociation, an overall charge of 0.50 e^-

has been transferred, mainly from the Fe_B to the OH group and from the protonated S to form a covalent bond with the H. This can be represented graphically in a charge density difference plot, illustrating electron density changes on the dissociative adsorption of a H_2O molecule. Figure 6 shows that charge is mostly localized on the O–H group and along the S–H bond. At state 2, the stretching mode (ν) of the adsorbed OH and incrusted SH groups are red-shifted with respect to the asymmetric (ν_{asym}) and symmetric (ν_{sym}) stretching modes of the respective isolated molecules. This indicates the weakening of the O–H bond, which together with the bending mode (δ) of the H–S–Fe and H–O–Fe groups support the H_2O dissociation on the $Fe_3S_4(001)$ surface, see Figure 7. We have found that configuration 2 is 0.34 eV above the reference energy (the pristine $Fe_3S_4(001)$ plus an isolated H_2O molecule). We have also tested unsuccessfully the possibility of complete H_2O splitting owing to the higher basicity of O^{2-} than S^{2-}. This behavior is similar to that found on the (001) surface of the isomorphic $FeNi_2S_4$.[66]

The reaction profile for the partial exchange of S by an O atom on the $Fe_3S_4(001)$ surface, according to mechanism 1, is shown in Figure 2. In this mechanism, only one H_2O molecule per unit cell is involved, equivalent to a coverage of 0.25 ML. Note that we have defined a full ML as the amount of H_2O
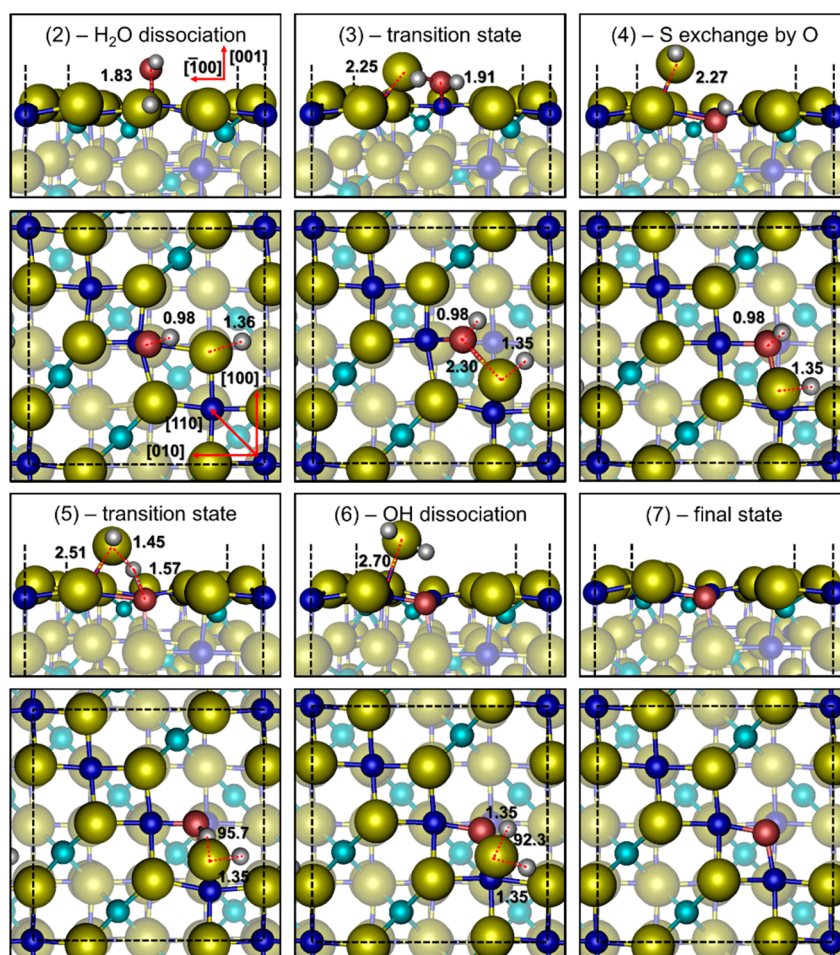
Figure 5. Top and side view of the structure of the numbered states along the $Fe_3S_4(001)$ surface oxidation pathway 1. Fe_A atoms are in light blue, Fe_B atoms are in dark blue, S atoms are in yellow, O atoms are in red, and H atoms are in white. Layers with atoms with dangling bonds are highlighted. Calculated bond distances (Å) and angles (deg) are also shown.
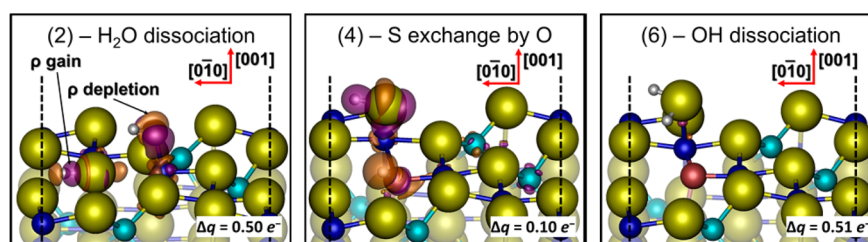

Figure 6. Charge density (ρ) flow for different stages along the oxidation of the $Fe_3S_4(001)$ surface following pathway 1. Electron density gain (depletion) surfaces are in orange (purple). Isosurfaces display a value of ± 0.05 e·Å^{-3}. Fe_A atoms are in light blue, Fe_B atoms are in dark blue, S atoms are in yellow, O atoms are in red, and H atoms are in white. Layers with atoms with dangling bonds are highlighted. Insets show the charge difference values.

required to hydrate all four Fe_B ions in the top surface layer per unit cell. In a concerted step, the SH group migrates to the top of the nearby Fe_B ion in the same layer, while O replaces S in the structure, thereby increasing its coordination number by three Fe ions. This is an exothermic process with an $E_{exch}^{O \rightarrow S}$ of −0.24 eV and an activation energy (E_{A3}) of 0.80 eV. Upon exchange of SH by OH, the O atom lies at 0.63 Å below the average position of the surface S atoms, in part due to its smaller ionic radius, see state 4 in Figure 5. Note that 0.44 Å is the difference in Shannon's radii between the hexacoordinated ions, S^{2-} and O^{2-}.[101] The O−H distance remains at 0.98 Å, with the H lying at the same level of the top S layer on the

cavity of the Fe_A row along the [110] direction. The charge analysis shows that during substitution of the labile SH by the more nucleophilic OH group, there is a transfer of 0.10 e$^-$ from the adsorbed S to the structural O. Figure 6 shows the charge transfer mechanism at the state 4 with respect to the oxidized surface and dissociated H_2S. In agreement with the atomic electronegativities, the electronic density located along the O−H bond comes primarily from the H, whereas the adsorbed SH relocates its electrons to the Fe_B−S and S−H bonds. At state 4, the vibrational mode of the OH group is red-shifted by 56.7 cm^{-1} and the SH group is blue-shifted by 118.8 cm^{-1} with respect to the IR bands of state 2, see Figure 7, parts a and b.
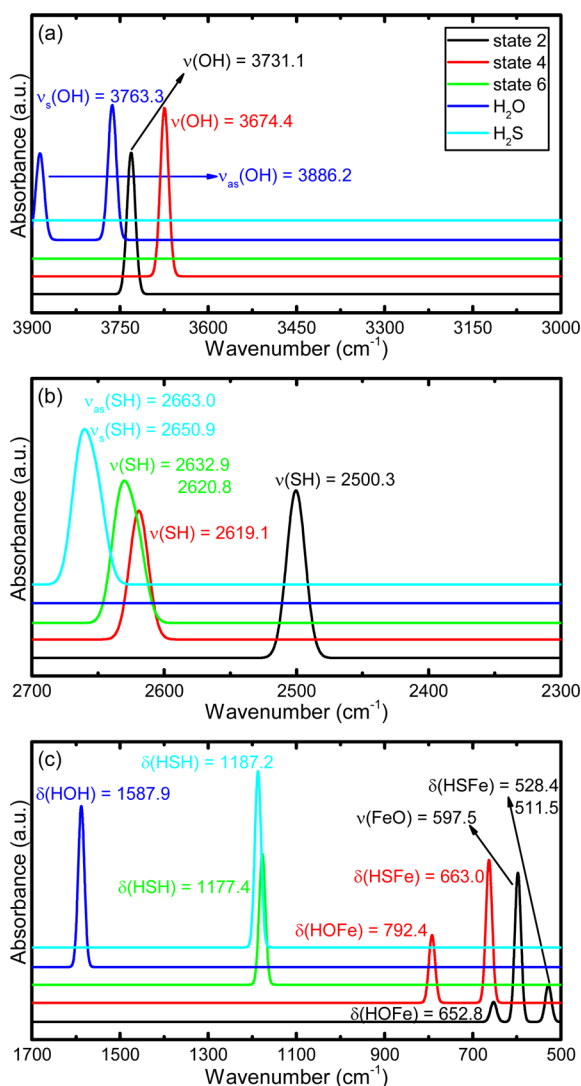
Figure 7. Simulated IR spectra of the reaction intermediates on the Fe$_3$S$_4$(001) surface for each state of pathway 1 and the isolated H$_2$O and H$_2$S molecules: (a) 3900−3000 cm^{-1} region, (b) 2700−2300 cm^{-1} region, and (c) 1700−500 cm^{-1} region. Presented vibrational modes are the asymmetric stretching (ν_{asym}), symmetric stretching (ν_{sym}), stretching (ν), and bending (δ) modes. Bands labeled with two numbers are composed by two overlapped peaks.

This further corroborates the weakening of the O−H bond and strengthening of the S−H bond, in agreement with the replacement of the structural SH group by the adsorbed OH group at the Fe$_3$S$_4$(001) surface. The Fe−O stretching mode vanishes, suggesting that this bond has become more ionic, i.e., a smaller dipole moment as the oxygen ion is now in the crystal lattice; see Figure 7, part c. The negligible absorbance of the Fe−S stretching mode is consistent with the low polarity of this bond.

The next step in this mechanism is the generation of H$_2$S following the migration of the adsorbed H, see state 6 in Figure 2. In the resulting structure, the O remains slightly below the top S layer, but moves horizontally by 0.81 Å closer to the Fe$_B$ ion holding the H$_2$S molecule. The H$_2$S molecule is adsorbed nearly vertically on top of the Fe$_B$ at 2.70 Å. The H atoms are at equal distances from the S (1.35 Å) forming a bond angle of 92.3°, i.e., very close to the ones calculated for the isolated molecule (1.35 Å and 92.1°) and found from microwave

spectroscopy (1.34 Å and 92.1°).[102] According to the charge analysis, the formation of the H$_2$S molecule is accompanied by a reduction of the charge of the migrating H by 0.51 e^-, which is provided by the SH and O−Fe$_B$−S groups (where S is next to O along the $[\overline{1}10]$ direction). Note that the fact that the charges of the two H atoms become very similar is an indication of the weak adsorption of the H$_2$S molecule, in agreement with the geometric similarities to the gas phase molecule. The step from state 4 to 6 is endothermic by 0.45 eV and its activation energy (E_{A5}) is 0.29 eV smaller than E_{A3} indicating that the OH−SH exchange is the determinant step in this pathway. At state 6, the O−H stretching mode disappears, in agreement with the dissociation of this bond, see Figure 7, part a. We have been able to detect the H$_2$S bending along with the asymmetric and symmetric stretching modes, corroborating the formation of this molecule, see Figure 7, parts b and c. The stretching bands are red-shifted with respect to the values calculated for the isolated molecule, suggesting that H$_2$S is interacting with the surface. H$_2$S desorption is an unfavorable process, as state 7 is 1.06 eV above the reference and 0.51 eV above state 6, which affects negligibly the surface structure and the charge of the atoms of the surface and H$_2$S. In the reverse process, the dissociation of a H$_2$S molecule adsorbed on a partially oxidized Fe$_3$S$_4$(001) has an activation energy of 0.06 eV, just above the thermal energy ($2k_BT$) at 298 K and therefore is thermodynamically and kinetically more favorable.

According to this pathway, the position for the S substitution was dictated by the most favorable H adsorption site. Nevertheless, the O moves to coordinate the Fe$_A$ next to the cavity along the $[110]$ direction in a solid state diffusion process that stabilizes the slab by an additional 0.14 eV after overcoming a barrier of 2.14 eV. This high activation energy for O diffusion suggests that this step is highly unlikely to take place under static conditions. In the structure of this final configuration, the O atom moved toward the vacuum by 0.21 Å but still remained below the S top layer. The charge analysis reveals that, after O diffusion, there has been 0.29 e^- charge transfer from the Fe$_B$ ions (from the surface and subsurface layers) formerly coordinating the O to the surface Fe$_B$ and Fe$_A$ ions currently coordinating the O atom, consistent with an oxidation state of 3+.

3.1.2. Pathway 2. A sensible alternative is to consider the H migration away from the Fe$_B$−OH center. This situation leads us to pathway 2, shown in Figure 3, which considers the partial oxidation of the surface by OH groups (coverage of 0.25 ML). Note that in agreement with the reference, the energies of states 2 to 6 have been calibrated by considering the energy of one proton located onto the most stable position on the Fe$_3$S$_4$(001) surface. We present the structures, charge density flow and IR spectra of the intermediates for pathways 2 and 3 in the Supporting Information, due to their similarities to pathway 1.

The hydroxylated surface, see stage 2 in Figure 3, is 0.09 eV lower in energy than the equivalent stage of pathway 1, corroborating the thermodynamic feasibility of the H migration. The Fe$_B$−O bond length is 0.02 Å shorter, see Figure SI-2, suggesting a slightly stronger interaction between these atoms in the absence of the second H atom, in agreement with the charge analysis shown in Figure SI-3.

In the absence of a protonated sulfur, the hydroxyl O replaces the S, leading to the most thermodynamically favorable product. The energy of this state is 0.15 eV lower than the reference system, in contrast to the 0.10 eV higher in pathway

1. The activation energy required to take our system from state 2 to 4 is 0.17 eV lower than in pathway 1; see Figure 3. The replaced S atom forms a hydrogen bond with the hydroxyl H; see state 4 in Figure SI-2. The O−H bond distance increases by 0.02 Å, while the O is displaced outward from the surface by 0.07 Å, as well as along the [110] direction, compared to the same stage in pathway 1. The Fe_B holding the adsorbed S atom is also moved along the [1$\bar{1}$0] direction. The charge analysis shows a rearrangement involving mainly the adsorbed S, the incorporated O and the Fe_A ion coordinating it; see Figure SI-3.

The next step along the oxidation process is the formation of the SH group. The protonated S moves to rest almost straight atop the Fe_B ion, which relaxes to its original position; see state 6 in Figure SI-2. The O atom moves horizontally along the [110] direction and outward from the surface by 0.11 Å. At this stage, the S−H bond length is equal to the one in states 4 and 6 of pathway 1, which is in agreement with the similar charge gain of the H in states 4 of pathways 1 and 2; see Figure SI-3. The OH dissociation process is endothermic by 0.79 eV making it the rate limiting step of pathway 2. The O−H dissociation is less favorable than the same process via pathway 1, both thermodynamically and kinetically.

The trend of changes in the vibrational frequencies of the intermediates in pathway 2 is similar to pathway 1; see Figure SI-4. However, the stretching and bending modes involving the H−S group are not detected in states 2 and 4 as no S atom is protonated. The Fe−O stretching mode can be detected in each reaction intermediate of pathway 2. This suggests that its dipole moment is different than in pathway 1, which agrees with the SH group interacting more strongly with the surface.

In the last step of pathway 2, the SH group interacts with a coadsorbed H atom, leading to the formation and desorption of the H_2S molecule, which leaves a partially oxidized surface slab in its most favorable geometry. We have also considered a variation of pathway 2, where the exchange of S by O takes place after the OH dissociation; see Figure 3. Nevertheless, the energies of the intermediates are higher than in the original pathway and therefore it is not representative as it is less likely to lead to Fe_3S_4(001) surface oxidation.

3.1.3. Pathway 3. Next, we have investigated the presence of a second H_2O molecule (0.50 ML) on the oxidation mechanism, see Figure 4. Previous work on the analogue spinel $FeNi_2S_4$ has suggested that the adsorption of a second H_2O molecule after dissociation of the first is most likely to take place on the Fe_B ion next to the protonated S, see state 2 in Figure SI-5.[66] The bond angle of the newly added H_2O is increased by 3.4° with respect to the calculated and experimental value for the isolated molecule.[102] The O−H bonds of the second H_2O molecule are 0.97 and 1.04 Å long. While the shortest length indicates no bond alteration,[102] the elongated OH bond is forming a hydrogen-bond with the neighboring hydroxyl group. The addition of a second H_2O molecule stabilized significantly the system, making this configuration the one with the lowest energy in this study.

In order to generate a second SH group within close proximity to a subsurface Fe_A ion, we have stretched the second H_2O until dissociation; see state 4 in Figure SI-5. The two SH groups are bridging both hydroxylated Fe_B ions, a configuration similar to the one found on $FeNi_2S_4$.[66] Hence, the new S−H bond is nearly perpendicular to the surface. The OH⋯OH hydrogen bond is stretched, leading to a reduction of the intrabond length. The configuration with two adsorbed OH groups and two surface SH is less thermodynamically stable

than state 2. The charge difference for the migrating H is similar to the value calculated in previous pathways, see Figure SI-6.

The protonated S binding the subsurface Fe_A is the most energetically favorable to be exchanged by an OH. After the exchange, the Fe_A ion holding the adsorbed SH group has migrated outward from the surface by 1.23 Å occupying an octahedral position; see state 6 in Figure SI-5. The structural OH group lies below the topmost atomic layer as in the two previously proposed pathways. An OH⋯OH distance of 1.38 Å indicates a hydrogen-bond between these OH groups, in agreement with the charge density flux plot of state 6 in Figure SI-6. The energy released during the SH to OH exchange step and the activation energy are the largest among the three pathways studied.

In the next step toward the Fe_3S_4(001) oxidation, the formation of a coadsorbed H_2O molecule takes place as a result of the deprotonation of the incorporated OH; see state 8 in Figure 4. This process is endothermic and requires the lowest activation energy barrier, making it the less demanding step among the three pathways. After the H migration, the surface O atom moves inward by 0.09 Å, while the H_2O moves away from the surface, almost presenting itself as an isolated molecule,[102] see Figure SI-5. The H_2O is tilted toward the adsorbed SH group, stablishing a weak hydrogen-bond, illustrated by the charge density difference plot, see Figure SI-6.

In the final step of the H_2S formation, one of the H atoms from the H_2O may migrate to the SH group, see state 10 in Figure 4. As this step is energetically and kinetically unfavorable, the SH groups are likely to remain in the surface, leading to their accumulation, similar to pathway 2. At this stage, the S of the H_2S molecule moves 0.18 Å outward and the Fe_B−O distance is reduced by 0.29 Å; see Figure SI-5. These results highlight the weak interaction between the H_2S molecule and the partially oxidized surface, which is corroborated in the charge density difference plot, see Figure SI-6.

The simulated IR spectra for pathway 3 are more complex than previous ones due to a larger number of intermediates, see Figure SI-7. For example, the IR spectrum of state 2 shows the O⋯H stretching mode associated with the OH⋯OH hydrogen bond at 2354.0 cm^{-1}. At states 2 and 8, the H−O−H torsion mode suggests a strong interaction of molecular H_2O with the surface. The duplicate stretching and bending modes involving the H−O and H−S are in agreement with two protonated O and S atoms.

Desorption of the H_2S molecule is an endothermic process, see state 11 in Figure 4. The release of the H_2S molecule is accompanied by the formation of a hydrogen-bond between the OH group and the surface O atom, see Figure SI-5. However, apart from this new interaction, the impact of the H_2S desorption on the surface structure is minimal.

The O diffusion process further stabilizes the system by 0.40 eV, i.e. nearly three times more exothermic than the solid diffusion process of pathway 1. However, the barrier to the transition state in pathway 3 is 6.6 times higher than in pathway 1, making this solid state transformation step less likely than in pathway 1. In the final configuration, the O occupies a position comparable to the one in the previously discussed pathways. There is, however, a lasting impact of the oxidation through the final mechanism on the position of the labile Fe_A ion, which remains in the octahedral cavity.

Table 2. Empirical Expressions for the First Ionization Constant of H_2S (K_{a1}), Vapor Pressure of H_2O (p_{H_2O}), and Henry Constant of H_2S (K_{H_2S}) as a Function of the Absolute Temperature

equation for constant	units of constant	ref
$\log(K_{a1}) = a_1 + a_2 T + a_3 T^2 + a_4 T^{-1} + a_5 \ln(T)$ $a_1 = 782.43945 \quad a_4 = -20565.7315$ $a_2 = 0.361261$ $a_3 = -1.6722 \cdot 10^{-4} \quad a_5 = -142.741722$	molality (mol·kg^{-1})	103
$\ln(p_{H_2O}) = \dfrac{T_c}{T}[b_1\tau + b_2\tau^{1.5} + b_3\tau^3 + b_4\tau^{3.5} + b_5\tau^4 + b_6\tau^{7.5}] + \ln(p_c)$ $T_c = 647.096\,K \quad b_2 = 1.84408259$ $p_c = 2.2064 \cdot 10^7\,Pa \quad b_3 = -11.7866497$ $\tau = 1 - \theta \quad b_4 = 22.6807411$ $\theta = \dfrac{T}{T_c} \quad b_5 = -15.9618719$ $b_1 = -7.85951783 \quad b_6 = 1.80122502$	Pa	106
$\log(K_{H_2S}) = c_1 + c_2 T + c_3 T^2 + c_4 T^{-1} + c_5 \log(T)$ $c_1 = -0.6342702616 \cdot 10^3 \quad c_4 = 0.1671907660 \cdot 10^5$ $c_2 = -0.2709284796$ $c_3 = 0.1113202904 \cdot 10^{-3} \quad c_5 = 0.2619219571 \cdot 10^3$	mol·bar^{-1}·kg^{-1}	107

3.2. Thermodynamics of H_2S and its Ionization Products in Aqueous Solution. Because of the interest in preventing H_2S release from iron−sulfur compounds, which leads to the acid mine drainage, we have investigated the equilibrium concentration of these species in aqueous solution. We have assumed that our system behaves ideally, which allows us to replace thermodynamic equilibrium constants by concentration quotients and activities by molal concentrations. We have calculated the concentration of aqueous H_2S from the oxidation of the $Fe_3S_4(001)$ surface and the pH of this solution as a function of temperature, in the range from 293 to 373 K. In order to calculate the concentrations of the species in aqueous solution in equilibrium with the pristine and partially oxidized $Fe_3S_4(001)$ surfaces, we have considered the process of partial oxidation of this surface by a H_2O molecule, according to eq 2, where the equilibrium constant (K_{o1}) is equal to the $[H_2S]$ in equilibrium with the solid phases.

$$Fe_{24}S_{32}(s) + H_2O(l) \underset{}{\overset{K_{o1}}{\rightleftharpoons}} Fe_{24}S_{31}O(s) + H_2S(aq) \qquad (2)$$
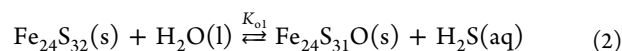
H_2S is a diprotic acid with two dissociation steps. The ionization constant of the first dissociation, represented by eq 3, is written as $K_{a1} = [H^+][SH^-][H_2S]^{-1}$ and its dependence on T at saturated water vapor pressure is shown in Table 2. We have not considered the second dissociation of H_2S as its constant K_{a2}[103] is at least 8 orders of magnitude smaller than K_{a1}[104] in the temperature range considered here. We have also ignored the autodissociation of H_2O as its ionic product (K_W) is also at least 6 orders of magnitude smaller than K_{a1} in the range of temperatures of interest.[105] Consequently, the $[H^+]$ is controlled by the first dissociation of H_2S, whereas the contribution of H^+ from the other processes is negligible.

$$H_2S(aq) \underset{}{\overset{K_{a1}}{\rightleftharpoons}} H^+(aq) + SH^-(aq) \qquad (3)$$
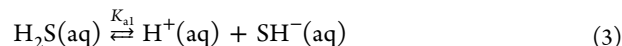
In order to link the gas phase state of the isolated molecules in our DFT simulations with the states in eq 2, we have

considered the vapor pressure of H_2O in equilibrium with its condensed phase and the solubility of gaseous H_2S in water. These processes are represented in eq 4 and 5, and their equilibrium constants are defined as p_{H_2O} and $K_{H_2S} = [H_2S]\,p_{H_2S}^{-1}$, respectively. The expressions of these equilibrium constants are also temperature-dependent and their empirical equations are shown in Table 2.

$$H_2O(l) \underset{}{\overset{p_{H_2O}}{\rightleftharpoons}} H_2O(g) \qquad (4)$$

$$H_2S(g) \underset{}{\overset{K_{H_2S}}{\rightleftharpoons}} H_2S(aq) \qquad (5)$$

The combination of eq 2, 4 and 5, leads to the reaction of the partial oxidation of the $Fe_3S_4(001)$ surface, eq 6 where H_2O and H_2S are in the reference state of our DFT calculations:

$$Fe_{24}S_{32}(s) + H_2O(g) \underset{}{\overset{K_o}{\rightleftharpoons}} Fe_{24}S_{31}O(s) + H_2S(g) \qquad (6)$$
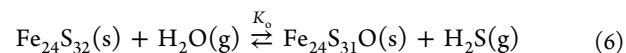
K_o is then calculated as shown in eq 7, from the Gibbs free energy (G) of the partial oxidation of the $Fe_3S_4(001)$ surface, where R and T are the ideal gas constant and the temperature of interest, respectively.

$$K_o = \frac{p_{H_2S}}{p_{H_2O}} = \frac{K_{o1}}{K_{H_2S} \cdot p_{H_2O}} = e^{-\Delta G^{\ominus}/RT} \qquad (7)$$

The change in the standard Gibbs free energy ($\Delta G^{\ominus}$) for the partial oxidation of the $Fe_3S_4(001)$ surface, according to eq 6, was calculated from $\Delta G^{\ominus} = \Delta H^{\ominus} - T\Delta S^{\ominus}$, where $\Delta H^{\ominus}$ is the enthalpy of this process, per H_2S molecule formed, $\Delta S^{\ominus}$ is the change in entropy and T is the temperature. The enthalpies of the three pathways investigated in this study are obtained directly from our calculations, where we assume that the enthalpy values do not depend on the temperature. We have additionally assumed that the entropies of the solid phases remain largely unchanged through the oxidation process and
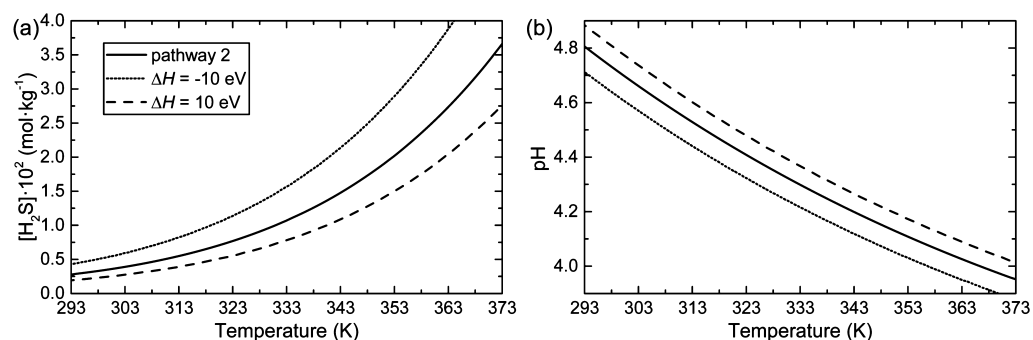
Figure 8. Calculated dependence of (a) [H_2S] and (b) pH with respect to T for the partial oxidation of the $Fe_3S_4(001)$ surface following pathway 2. The dotted and dashed lines are added for comparison purposes, representing processes with $\Delta H^\ominus = -10$ and 10 eV respectively.

that only the change in entropy due to the replacement of gaseous H_2O by H_2S is necessary to take into account. Similar considerations have been used to explain the dehydration of a number of α-FeO(OH) and α-Fe_2O_3 surfaces[108] and the dissolution/nucleation process at the α-quartz (0001) surface in liquid water.[109] We have used the entropies of H_2O and H_2S calculated at different temperatures using statistical thermodynamics.[67,110−112] For a comparison between the experimental and calculated values of entropy of these molecules, see Figure SI-8. Combining K_o, as shown in eq 7, with the expressions for K_{H_2S} and p_{H_2O} from Table 2, it is possible to determine K_{o1} and therefore [H_2S] as a function of the temperature when H_2O is in the liquid state and H_2S is dissolved in water.

The partial oxidation of the $Fe_3S_4(001)$ surface in a wet environment, represented by the concentration of H_2S as a function of the temperature, is shown in Figure 8, part a. This graph only shows the curve associated with pathway 2 ($\Delta H^\ominus = 0.92$ eV), which is the most kinetically and thermodynamically favorable, since the curves related to the other the pathways are almost coincident with this one. As expected from an endothermic process, the increment of temperature brings an exponential increase of the concentration of products: [H_2S] is equal to $2.77 \cdot 10^{-3}$ mol·kg^{-1} at $T = 293$ K and $3.65 \cdot 10^{-2}$ mol·kg^{-1} at $T = 393$ K. Figure 8, part b, shows how the pH decreases with temperature, as is also expected from a solution with an increasing concentration of a weak acid. In Figure 8, parts a and b, we have also added two auxiliary lines showing the behavior of hypothetical pathways whose $\Delta H^\ominus$ are approximately ±10 times bigger than pathway 2. These lines illustrate how noticeably the enthalpy of the process affects the dependence of [H_2S] and pH with T. The trend of pH with respect to temperature shown in Figure 8, part b, is therefore also valid for any sulfide that dissolves in H_2O through an oxidation mechanism with an enthalpy within the range -10.0 to $+10.0$ eV. As the experimental pH = 4.03 of a solution of Fe_3S_4 at 25 °C[41] apparently increases by the effect of the more soluble coexisting FeS phase,[49] our results agree with this expectation. Figure 8, part b, shows that the initial oxidation stages of pure Fe_3S_4 by H_2O will produce a solution with pH = 4.7 at 25 °C. Since the pH is always below 4.81 in the range of temperatures from 293 to 373 K and large Fe_3S_4 deposits are present in aquatic environments, from our calculations it would appear that these mineral deposits could be significant contributors to acid mine drainage.

4. CONCLUSIONS

In this paper, we have proposed and modeled three different pathways for the early steps of the $Fe_3S_4(001)$ surface oxidation promoted by H_2O. We have used DFT methods with a Hubbard Hamiltonian and empirical long-range dispersion corrections to calculate the reactants, products, intermediates and transition states in the thermodynamic and kinetic energy profiles. In each of these mechanisms, a surface S atom is replaced by an O atom from H_2O, producing a H_2S molecule. We have found that the step where the OH group replaces the S atom always take place before the OH deprotonation. However, for pathway 2, we could also model an alternative reaction route, but there all intermediates and transition states were between 1.56 and 0.37 eV higher in energy than in the former mechanism. We have found that pathways 1 and 2 are the most effective routes to initiate the $Fe_3S_4(001)$ surface oxidation. Although in pathway 1 the total $\Delta H^\ominus$ (per H_2S molecule) is 0.14 eV higher than in pathway 2, the rate-determining step in pathway 1 is 0.41 eV smaller than in pathway 2. The presence of the dissociated H^+ from the H_2O in the vicinity of the reactive site in pathway 1 directs the oxidation reaction toward a kinetic product where the solid state exchange of S by O becomes the step with the highest activation energy. On the other hand, the absence of the dissociated H^+ in the vicinity of the reactive site in pathway 2 leads to the most thermodynamically favorable oxidized state and the O−H dissociation becomes the rate-limiting step. When two H_2O molecules are adsorbed near the reactive center, pathway 3, they direct the oxidation reaction to a kinetic product 0.42 eV higher in energy than the one obtained in pathway 1. The highest activation energy calculated in this study is associated with the dissociation of the second H_2O molecule in pathway 3, making this an unlikely process. For any of the proposed mechanisms, H migration (i.e., from H_2O or OH) and H_2S desorption are endothermic processes, while the introduction of the OH group on the surface is an exothermic step. The energy balance of these processes, especially for pathway 2 operating under basic conditions, makes the partially oxidized $Fe_3S_4(001)$ surface likely to remain hydroxylated as this is the most stable intermediate. Changes in the values of the wave numbers of the calculated normal vibrational modes of the adsorbed intermediates indicate their transformation. The calculated [H_2S] in aqueous solution, and therefore pH, in chemical equilibrium with the solid phases at a range of temperatures, shows that Fe_3S_4 may be among those minerals responsible for acid mine or rock drainage.

Future work will include the consideration of the Fe_3S_4 oxidation by O_2 and a mixture of H_2O and O_2. In addition, we

will also carry out a microkinetic analysis of all the steps taking place during the initial oxidation stages of Fe_3S_4, which will allow us to include temperature and concentration effects and will mimic the dissolution of this mineral within a realistic processes framework.

■ ASSOCIATED CONTENT

Ⓢ Supporting Information

The Supporting Information is available free of charge on the ACS Publications website at DOI: 10.1021/acs.jpcc.6b00216.

Table showing the experimental and optimized lattice and sulfur parameters, total magnetization of saturation, and the atomic spin moments and atomic charges of bulk Fe_3S_4, graphs showing the density of states of the bulk and (001) surface of Fe_3S_4, and a graph showing the experimental and calculated entropy of gaseous H_2S and H_2O molecules (PDF)

■ AUTHOR INFORMATION

Corresponding Authors

*(D.S.-C.) Telephone: +44 (0)29 2087 0827. E-mail: SantosCarballalD@cardiff.ac.uk.
*(N.H.d.L.) Telephone: +44 (0)29 2087 0658. E-mail: deLeeuwN@cardiff.ac.uk.

Notes

The authors declare no competing financial interest.

■ ACKNOWLEDGMENTS

■ REFERENCES

(1) Joeckel, R. M.; Ang Clement, B. J.; VanFleet Bates, L. R. Sulfate-Mineral Crusts from Pyrite Weathering and Acid Rock Drainage in the Dakota Formation and Graneros Shale, Jefferson County, Nebraska. *Chem. Geol.* **2005**, *215* (1−4), 433−452.

(2) Banks, D.; Younger, P. L.; Arnesen, R.-T.; Iversen, E. R.; Banks, S. B. Mine-Water Chemistry: The Good, the Bad and the Ugly. *Environ. Geol.* **1997**, *32* (3), 157−174.

(3) Bowen, G. G.; Dussek, C.; Hamilton, R. M. Pollution Resulting from the Abandonment and Subsequent Flooding of Wheal Jane Mine in Cornwall, UK. In *Groundwater Contaminants and their Migration*; Mather, J., Banks, D., Dumpleton, S., Fermor, M., Eds.; Special Publications, Geological Society: London, 1998; Vol. *128*, pp 93−99.

(4) Younger, P. L. Mine Water Pollution from Kernow to Kwazulu-Natal: Geochemical Remedial Options and Their Selection in Practice. *Geosci. South-West Engl.* **2002**, *10* (3), 255−266.

(5) Johnson, D. B. Chemical and Microbiological Characteristics of Mineral Spoils and Drainage Waters at Abandoned Coal and Metal Mines. *Water, Air, Soil Pollut.: Focus* **2003**, *3* (1), 47−66.

(6) Schippers, A.; Sand, W. Bacterial Leaching of Metal Sulfides Proceeds by Two Indirect Mechanisms via Thiosulfate or via Polysulfides and Sulfur. *Appl. Environ. Microbiol.* **1999**, *65* (1), 319−321.

(7) Fowler, T. A.; Holmes, P. R.; Crundwell, F. K. Mechanism of Pyrite Dissolution in the Presence of Thiobacillus Ferrooxidans. *Appl. Environ. Microbiol.* **1999**, *65* (7), 2987−2993.

(8) Fowler, T. A.; Holmes, P. R.; Crundwell, F. K. On the Kinetics and Mechanism of the Dissolution of Pyrite in the Presence of Thiobacillus Ferrooxidans. *Hydrometallurgy* **2001**, *59* (2−3), 257−270.

(9) Hammarstrom, J. M.; Sibrell, P. L.; Belkin, H. E. Characterization of Limestone Reacted with Acid-Mine Drainage in a Pulsed Limestone Bed Treatment System at the Friendship Hill National Historical Site, Pennsylvania, USA. *Appl. Geochem.* **2003**, *18* (11), 1705−1721.

(10) Matlock, M. M.; Howerton, B. S.; Atwood, D. A. Chemical Precipitation of Heavy Metals from Acid Mine Drainage. *Water Res.* **2002**, *36* (19), 4757−4764.

(11) Vaughan, D. J.; Craig, J. R. *Mineral Chemistry of Metal Sulfides*; Cambridge University Press: Cambridge, U.K., 1978.

(12) Morse, J.; Millero, F.; Cornwell, J.; Rickard, D. The Chemistry of the Hydrogen Sulfide and Iron Sulfide Systems in Natural Waters. *Earth-Sci. Rev.* **1987**, *24* (1), 1−42.

(13) Akcil, A.; Koldas, S. Acid Mine Drainage (AMD): Causes, Treatment and Case Studies. *J. Cleaner Prod.* **2006**, *14* (12−13), 1139−1145.

(14) Johnson, D. B.; Hallberg, K. B. Acid Mine Drainage Remediation Options: A Review. *Sci. Total Environ.* **2005**, *338* (1−2), 3−14.

(15) Berner, R. A. Sedimentary Pyrite Formation: An Update. *Geochim. Cosmochim. Acta* **1984**, *48* (4), 605−615.

(16) Berner, R. A. Sedimentary Pyrite Formation. *Am. J. Sci.* **1970**, *268* (1), 1−23.

(17) McKibben, M. A.; Barnes, H. L. Oxidation of Pyrite in Low Temperature Acidic Solutions: Rate Laws and Surface Textures. *Geochim. Cosmochim. Acta* **1986**, *50* (7), 1509−1520.

(18) Moses, C. O.; Kirk Nordstrom, D.; Herman, J. S.; Mills, A. L. Aqueous Pyrite Oxidation by Dissolved Oxygen and by Ferric Iron. *Geochim. Cosmochim. Acta* **1987**, *51* (6), 1561−1571.

(19) Lowson, R. T. Aqueous Oxidation of Pyrite by Molecular Oxygen. *Chem. Rev.* **1982**, *82* (5), 461−497.

(20) Rimstidt, J. D.; Vaughan, D. J. Pyrite Oxidation: A State-of-the-Art Assessment of the Reaction Mechanism. *Geochim. Cosmochim. Acta* **2003**, *67* (5), 873−880.

(21) Williamson, M. A.; Rimstidt, J. D. The Kinetics and Electrochemical Rate-Determining Step of Aqueous Pyrite Oxidation. *Geochim. Cosmochim. Acta* **1994**, *58* (24), 5443−5454.

(22) Gartman, A.; Luther, G. W. Oxidation of Synthesized Sub-Micron Pyrite (FeS_2) in Seawater. *Geochim. Cosmochim. Acta* **2014**, *144*, 96−108.

(23) Chandra, A. P.; Gerson, A. R. The Mechanisms of Pyrite Oxidation and Leaching: A Fundamental Perspective. *Surf. Sci. Rep.* **2010**, *65* (9), 293−315.

(24) Wilkin, R. T.; Barnes, H. L. Pyrite Formation by Reactions of Iron Monosulfides with Dissolved Inorganic and Organic Sulfur Species. *Geochim. Cosmochim. Acta* **1996**, *60* (21), 4167−4179.

(25) Benning, L. G.; Wilkin, R. T.; Barnes, H. L. Reaction Pathways in the Fe−S System below 100°C. *Chem. Geol.* **2000**, *167* (1−2), 25−51.

(26) Lennie, A. R.; Redfern, S. A. T.; Champness, P. E.; Stoddart, C. P.; Schofield, P. F.; Vaughan, D. J. Transformation of Mackinawite to Greigite: An in Situ X-Ray Powder Diffraction and Transmission Electron Microscope Study. *Am. Mineral.* **1997**, *82* (3−4), 302−309.

(27) Dekkers, M. J.; Schoonen, M. A. A. Magnetic Properties of Hydrothermally Synthesized Greigite (Fe₃S₄)-I. Rock Magnetic Parameters at Room Temperature. *Geophys. J. Int.* **1996**, *126* (2), 360−368.

(28) Hunger, S.; Benning, L. G. Greigite: A True Intermediate on the Polysulfide Pathway to Pyrite. *Geochem. Trans.* **2007**, *8*, 1.

(29) Stolz, J. F.; Chang, S.-B. R.; Kirschvink, J. L. Magnetotactic Bacteria and Single-Domain Magnetite in Hemipelagic Sediments. *Nature* **1986**, *321* (6073), 849−851.

(30) Roberts, A. P.; Turner, G. M. Diagenetic Formation of Ferrimagnetic Iron Sulphide Minerals in Rapidly Deposited Marine Sediments, South Island, New Zealand. *Earth Planet. Sci. Lett.* **1993**, *115* (1−4), 257−273.

(31) Jelinowska, A.; Tucholka, P.; Guichard, F.; Lefèvre, I.; Badaut-Trauth, D.; Chalié, F.; Gasse, F.; Tribovillard, N.; Desprairies, A. Mineral Magnetic Study of Late Quaternary South Caspian Sea Sediments: Palaeoenvironmental Implications. *Geophys. J. Int.* **1998**, *133* (2), 499−509.

(32) Snowball, I. F. Magnetic Hysteresis Properties of Greigite (Fe₃S₄) and a New Occurrence in Holocene Sediments from Swedish Lappland. *Phys. Earth Planet. Inter.* **1991**, *68* (1−2), 32−40.

(33) Jelinowska, A.; Tucholka, P.; Gasse, F.; Fontes, J. C. Mineral Magnetic Record of Environment in Late Pleistocene and Holocene Sediments, Lake Manas, Xinjiang, China. *Geophys. Res. Lett.* **1995**, *22* (8), 953−956.

(34) Frank, U.; Nowaczyk, N. R.; Negendank, J. F. W. Palaeomagnetism of Greigite Bearing Sediments from the Dead Sea, Israel. *Geophys. J. Int.* **2007**, *168* (3), 904−920.

(35) Skinner, B. J.; Erd, R. C.; Grimaldi, F. S. Greigite, the Thio-Spinel of Iron; a New Mineral. *Am. Mineral.* **1964**, *49* (5−6), 543−555.

(36) Fassbinder, J. W. E.; Stanjek, H. Magnetic Properties of Biogenic Soil Greigite (Fe₃S₄). *Geophys. Res. Lett.* **1994**, *21* (22), 2349−2352.

(37) Fassbinder, J. W. E.; Stanjek, H.; Vali, H. Occurrence of Magnetic Bacteria in Soil. *Nature* **1990**, *343* (6254), 161−163.

(38) Mann, S.; Sparks, N. H. C.; Frankel, R. B.; Bazylinski, D. A.; Jannasch, H. W. Biomineralization of Ferrimagnetic Greigite (Fe₃S₄) and Iron Pyrite (FeS₂) in a Magnetotactic Bacterium. *Nature* **1990**, *343* (6255), 258−261.

(39) Goffredi, S. K.; Waren, A.; Orphan, V. J.; Van Dover, C. L.; Vrijenhoek, R. C. Novel Forms of Structural Integration between Microbes and a Hydrothermal Vent Gastropod from the Indian Ocean. *Appl. Environ. Microbiol.* **2004**, *70* (5), 3082−3090.

(40) Cornwell, J. C.; Morse, J. W. The Characterization of Iron Sulfide Minerals in Anoxic Marine Sediments. *Mar. Chem.* **1987**, *22* (2−4), 193−206.

(41) Berner, R. A. Thermodynamic Stability of Sedimentary Iron Sulfides. *Am. J. Sci.* **1967**, *265* (9), 773−785.

(42) Allen, R. E.; Parkes, R. J. Digestion Procedures for Determining Reduced Sulfur Species in Bacterial Cultures and in Ancient and Recent Sediments. In *Geochemical Transformations of Sedimentary Sulfur*; Vairavamurthy, M. A., Schoonen, M. A. A., Eglinton, T. I., Luther, G. W., III, Manowitz, B., Eds.; ACS Symposium Series 612; American Chemical Society: Washington DC, 1995; pp 243−257.

(43) Popa, R.; Kinkle, B. K. Discrimination among Iron Sulfide Species Formed in Microbial Cultures. *J. Microbiol. Methods* **2000**, *42* (2), 167−174.

(44) Ulrich, G. A.; Krumholz, L. R.; Suflita, J. M. A Rapid and Simple Method for Estimating Sulfate Reduction Activity and Quantifying Inorganic Sulfides. *Appl. Environ. Microbiol.* **1997**, *63* (11), 4626.

(45) Fossing, H.; Jorgensen, B. B. Chromium Reduction Method of Bacterial Sulfate Reduction in Sediments: Measurement Reduction of a Single-Step Chromium Method Evaluation. *Biogeochemistry* **1989**, *8* (3), 205−222.

(46) Canfield, D. E.; Raiswell, R.; Westrich, J. T.; Reaves, C. M.; Berner, R. A. The Use of Chromium Reduction in the Analysis of Reduced Inorganic Sulfur in Sediments and Shales. *Chem. Geol.* **1986**, *54*, 149−155.

(47) Neretin, L. N.; Böttcher, M. E.; Jørgensen, B. B.; Volkov, I. I.; Lüschen, H.; Hilgenfeldt, K. Pyritization Processes and Greigite Formation in the Advancing Sulfidization Front in the Upper Pleistocene Sediments of the Black Sea. *Geochim. Cosmochim. Acta* **2004**, *68* (9), 2081−2093.

(48) Lyons, T. W.; Werne, J. P.; Hollander, D. J.; Murray, R. W. Contrasting Sulfur Geochemistry and Fe/Al and Mo/Al Ratios across the Last Oxic-to-Anoxic Transition in the Cariaco Basin, Venezuela. *Chem. Geol.* **2003**, *195* (1−4), 131−157.

(49) Rickard, D.; Luther, G. W., III Chemistry of Iron Sulfides. *Chem. Rev. (Washington, DC, U. S.)* **2007**, *107* (2), 514−562.

(50) Roldan, A.; Hollingsworth, N.; Roffey, A.; Islam, H.-U.; Goodall, J. B. M.; Catlow, C. R. A.; Darr, J. A.; Bras, W.; Sankar, G.; Holt, K. B.; et al. Bio-Inspired CO₂ Conversion by Iron Sulfide Catalysts under Sustainable Conditions. *Chem. Commun.* **2015**, *51* (35), 7501−7504.

(51) Kresse, G.; Hafner, J. Ab Initio Molecular Dynamics for Liquid Metals. *Phys. Rev. B: Condens. Matter Mater. Phys.* **1993**, *47* (1), 558−561.

(52) Kresse, G.; Hafner, J. Ab Initio Molecular-Dynamics Simulation of the Liquid-Metal−Amorphous-Semiconductor Transition in Germanium. *Phys. Rev. B: Condens. Matter Mater. Phys.* **1994**, *49* (20), 14251−14269.

(53) Kresse, G.; Furthmüller, J. Efficiency of Ab-Initio Total Energy Calculations for Metals and Semiconductors Using a Plane-Wave Basis Set. *Comput. Mater. Sci.* **1996**, *6* (1), 15−50.

(54) Kresse, G.; Furthmüller, J. Efficient Iterative Schemes for Ab Initio Total-Energy Calculations Using a Plane-Wave Basis Set. *Phys. Rev. B: Condens. Matter Mater. Phys.* **1996**, *54* (16), 11169−11186.

(55) Kresse, G.; Joubert, D. From Ultrasoft Pseudopotentials to the Projector Augmented-Wave Method. *Phys. Rev. B: Condens. Matter Mater. Phys.* **1999**, *59* (3), 1758−1775.

(56) Blöchl, P. E. Projector Augmented-Wave Method. *Phys. Rev. B: Condens. Matter Mater. Phys.* **1994**, *50* (24), 17953−17979.

(57) Perdew, J. P.; Chevary, J. A.; Vosko, S. H.; Jackson, K. A.; Pederson, M. R.; Singh, D. J.; Fiolhais, C. Atoms, Molecules, Solids, and Surfaces: Applications of the Generalized Gradient Approximation for Exchange and Correlation. *Phys. Rev. B: Condens. Matter Mater. Phys.* **1992**, *46* (11), 6671−6687.

(58) Perdew, J. P.; Chevary, J. A.; Vosko, S. H.; Jackson, K. A.; Pederson, M. R.; Singh, D. J.; Fiolhais, C. Erratum: Atoms, Molecules, Solids, and Surfaces: Applications of the Generalized Gradient Approximation for Exchange and Correlation. *Phys. Rev. B: Condens. Matter Mater. Phys.* **1993**, *48* (7), 4978−4978.

(59) Vosko, S. H.; Wilk, L.; Nusair, M. Accurate Spin-Dependent Electron Liquid Correlation Energies for Local Spin Density Calculations: A Critical Analysis. *Can. J. Phys.* **1980**, *58* (8), 1200−1211.

(60) Grimme, S. Semiempirical GGA-Type Density Functional Constructed with a Long-Range Dispersion Correction. *J. Comput. Chem.* **2006**, *27* (15), 1787−1799.

(61) Perdew, J. P.; Burke, K.; Ernzerhof, M. Generalized Gradient Approximation Made Simple [Phys. Rev. Lett. 77, 3865 (1996)]. *Phys. Rev. Lett.* **1997**, *78* (7), 1396−1396.

(62) Perdew, J. P.; Burke, K.; Ernzerhof, M. Generalized Gradient Approximation Made Simple. *Phys. Rev. Lett.* **1996**, *77* (18), 3865−3868.

(63) Terranova, U.; de Leeuw, N. H. Aqueous Fe₂S₂ Cluster: Structure, Magnetic Coupling, and Hydration Behaviour from Hubbard U Density Functional Theory. *Phys. Chem. Chem. Phys.* **2014**, *16* (26), 13426−13433.

(64) Dzade, N. Y.; Roldan, A.; de Leeuw, N. H. The Surface Chemistry of NOₓ on Mackinawite (FeS) Surfaces: A DFT-D2 Study. *Phys. Chem. Chem. Phys.* **2014**, *16* (29), 15444−15456.

(65) Santos-Carballal, D.; Roldan, A.; Grau-Crespo, R.; de Leeuw, N. H. First-Principles Study of the Inversion Thermodynamics and Electronic Structure of FeM$_2$X$_4$ (thio)spinels (M = Cr, Mn, Co, Ni; X = O, S). *Phys. Rev. B: Condens. Matter Mater. Phys.* **2015**, *91* (19), 195106.

(66) Haider, S.; Roldan, A.; de Leeuw, N. H. Catalytic Dissociation of Water on the (001), (011), and (111) Surfaces of Violarite, FeNi$_2$S$_4$: A DFT-D2 Study. *J. Phys. Chem. C* **2014**, *118* (4), 1958−1967.

(67) Dzade, N. Y.; Roldan, A.; de Leeuw, N. H. Adsorption of Methylamine on Mackinawite (FES) Surfaces: A Density Functional Theory Study. *J. Chem. Phys.* **2013**, *139* (12), 124708.

(68) Dzade, N. Y.; Roldan, A.; de Leeuw, N. H. Activation and Dissociation of CO$_2$ on the (001), (011), and (111) Surfaces of Mackinawite (FeS): A Dispersion-Corrected DFT Study. *J. Chem. Phys.* **2015**, *143* (9), 094703.

(69) Monkhorst, H. J.; Pack, J. D. Special Points for Brillouin-Zone Integrations. *Phys. Rev. B* **1976**, *13* (12), 5188−5192.

(70) Blöchl, P. E.; Jepsen, O.; Andersen, O. K. Improved Tetrahedron Method for Brillouin-Zone Integrations. *Phys. Rev. B: Condens. Matter Mater. Phys.* **1994**, *49* (23), 16223−16233.

(71) Anisimov, V. I.; Korotin, M. A.; Zaanen, J.; Andersen, O. K. Spin Bags, Polarons, and Impurity Potentials in La$_{2-x}$Sr$_x$CuO$_4$ from First Principles. *Phys. Rev. Lett.* **1992**, *68* (3), 345−348.

(72) Dudarev, S. L.; Botton, G. A.; Savrasov, S. Y.; Humphreys, C. J.; Sutton, A. P. Electron-Energy-Loss Spectra and the Structural Stability of Nickel Oxide: An LSDA+U Study. *Phys. Rev. B: Condens. Matter Mater. Phys.* **1998**, *57* (3), 1505−1509.

(73) Devey, A. J.; Grau-Crespo, R.; de Leeuw, N. H. Electronic and Magnetic Structure of Fe$_3$S$_4$: GGA+U Investigation. *Phys. Rev. B: Condens. Matter Mater. Phys.* **2009**, *79* (19), 195126.

(74) Roldan, A.; Santos-Carballal, D.; de Leeuw, N. H. A Comparative DFT Study of the Mechanical and Electronic Properties of Greigite Fe$_3$S$_4$ and Magnetite Fe$_3$O$_4$. *J. Chem. Phys.* **2013**, *138* (20), 204712.

(75) Haider, S.; Grau-Crespo, R.; Devey, A. J.; de Leeuw, N. H. Cation Distribution and Mixing Thermodynamics in Fe/Ni Thiospinels. *Geochim. Cosmochim. Acta* **2012**, *88*, 275−282.

(76) Heyden, A.; Bell, A. T.; Keil, F. J. Efficient Methods for Finding Transition States in Chemical Reactions: Comparison of Improved Dimer Method and Partitioned Rational Function Optimization Method. *J. Chem. Phys.* **2005**, *123* (22), 224101.

(77) Henkelman, G.; Jónsson, H. A Dimer Method for Finding Saddle Points on High Dimensional Potential Surfaces Using Only First Derivatives. *J. Chem. Phys.* **1999**, *111* (15), 7010−7022.

(78) Surerus, K. K.; Kennedy, M. C.; Beinert, H.; Münck, E. Mössbauer Study of the Inactive Fe$_3$S$_4$ and Fe$_3$Se$_4$ and the Active Fe$_4$Se$_4$ Forms of Beef Heart Aconitase. *Proc. Natl. Acad. Sci. U. S. A.* **1989**, *86* (24), 9846−9850.

(79) Vaughan, D. J.; Craig, J. R. The Crystal Chemistry of Iron-Nickel Thiospinels. *Am. Mineral.* **1985**, *70* (9-10), 1036−1043.

(80) Vaughan, D. J.; Tossell, J. A. Electronic Structure of Thiospinel Minerals: Results from MO Calculation. *Am. Mineral.* **1981**, *66* (11−12), 1250−1253.

(81) Chang, L.; Rainford, B. D.; Stewart, J. R.; Ritter, C.; Roberts, A. P.; Tang, Y.; Chen, Q. Magnetic Structure of Greigite (Fe$_3$S$_4$) Probed by Neutron Powder Diffraction and Polarized Neutron Diffraction. *J. Geophys. Res.* **2009**, *114* (B7), B07101.

(82) Dekkers, M. J.; Passier, H. F.; Schoonen, M. A. A. Magnetic Properties of Hydrothermally Synthesized Greigite (Fe$_3$S$_4$)−II. High- and Low-Temperature Characteristics. *Geophys. J. Int.* **2000**, *141* (3), 809−819.

(83) Tasker, P. W. The Stability of Ionic Crystal Surfaces. *J. Phys. C: Solid State Phys.* **1979**, *12* (22), 4977−4984.

(84) Santos-Carballal, D.; Roldan, A.; Grau-Crespo, R.; de Leeuw, N. H. A DFT Study of the Structures, Stabilities and Redox Behaviour of the Major Surfaces of Magnetite Fe$_3$O$_4$. *Phys. Chem. Chem. Phys.* **2014**, *16* (39), 21082−21097.

(85) Asara, G. G.; Roldan, A.; Ricart, J. M.; Rodriguez, J. A.; Illas, F.; de Leeuw, N. H. New Insights into the Structure of the C-Terminated β-Mo$_2$C (001) Surface from First-Principles Calculations. *J. Phys. Chem. C* **2014**, *118* (33), 19224−19231.

(86) Cadi-Essadek, A.; Roldan, A.; de Leeuw, N. H. Ni Deposition on Yttria-Stabilized ZrO$_2$(111) Surfaces: A Density Functional Theory Study. *J. Phys. Chem. C* **2015**, *119* (12), 6581−6591.

(87) Devey, A. J.; Grau-Crespo, R.; de Leeuw, N. H. Combined Density Functional Theory and Interatomic Potential Study of the Bulk and Surface Structures and Properties of the Iron Sulfide Mackinawite (FeS). *J. Phys. Chem. C* **2008**, *112* (29), 10960−10967.

(88) Shields, A. E.; Santos-Carballal, D.; de Leeuw, N. H. A Density Functional Theory Study of Uranium-Doped Thoria and Uranium Adatoms on the Major Surfaces of Thorium Dioxide. *J. Nucl. Mater.* **2016**, *473*, 99−111.

(89) Makov, G.; Payne, M. C. Periodic Boundary Conditions in Ab Initio Calculations. *Phys. Rev. B: Condens. Matter Mater. Phys.* **1995**, *51* (7), 4014−4022.

(90) Neugebauer, J.; Scheffler, M. Adsorbate-Substrate and Adsorbate-Adsorbate Interactions of Na and K Adlayers on Al(111). *Phys. Rev. B: Condens. Matter Mater. Phys.* **1992**, *46* (24), 16067−16080.

(91) Henkelman, G.; Arnaldsson, A.; Jónsson, H. A Fast and Robust Algorithm for Bader Decomposition of Charge Density. *Comput. Mater. Sci.* **2006**, *36* (3), 354−360.

(92) Sanville, E.; Kenny, S. D.; Smith, R.; Henkelman, G. Improved Grid-Based Algorithm for Bader Charge Allocation. *J. Comput. Chem.* **2007**, *28* (5), 899−908.

(93) Tang, W.; Sanville, E.; Henkelman, G. A Grid-Based Bader Analysis Algorithm without Lattice Bias. *J. Phys.: Condens. Matter* **2009**, *21* (8), 084204.

(94) Irikura, K. K.; Johnson, R. D.; Kacker, R. N. Uncertainties in Scaling Factors for Ab Initio Vibrational Frequencies. *J. Phys. Chem. A* **2005**, *109* (37), 8430−8437.

(95) Pople, J. A.; Scott, A. P.; Wong, M. W.; Radom, L. Scaling Factors for Obtaining Fundamental Vibrational Frequencies and Zero-Point Energies from HF/6-31G* and MP2/6-31G* Harmonic Frequencies. *Isr. J. Chem.* **1993**, *33* (3), 345−350.

(96) Wong, M. W. Vibrational Frequency Prediction Using Density Functional Theory. *Chem. Phys. Lett.* **1996**, *256* (4−5), 391−399.

(97) Scott, A. P.; Radom, L. Harmonic Vibrational Frequencies: An Evaluation of Hartree−Fock, Møller−Plesset, Quadratic Configuration Interaction, Density Functional Theory, and Semiempirical Scale Factors. *J. Phys. Chem.* **1996**, *100* (41), 16502−16513.

(98) Halls, M. D.; Velkovski, J.; Schlegel, H. B. Harmonic Frequency Scaling Factors for Hartree-Fock, S-VWN, B-LYP, B3-LYP, B3-PW91 and MP2 with the Sadlej pVTZ Electric Property Basis Set. *Theor. Chem. Acc.* **2001**, *105* (6), 413−421.

(99) Shimanouchi, T. Tables of Molecular Vibrational Frequencies Consolidated Volume I. *Natl. Stand. Ref. Data Syst. Natl. Bur. Stand.* **1976**, *39*, 164.

(100) de Leeuw, N. H.; Parker, S. Molecular-Dynamics Simulation of MgO Surfaces in Liquid Water Using a Shell-Model Potential for Water. *Phys. Rev. B: Condens. Matter Mater. Phys.* **1998**, *58* (20), 13901−13908.

(101) Shannon, R. D. Revised Effective Ionic Radii and Systematic Studies of Interatomic Distances in Halides and Chalcogenides. *Acta Crystallogr., Sect. A: Cryst. Phys., Diffr., Theor. Gen. Crystallogr.* **1976**, *32* (5), 751−767.

(102) Harmony, M. D.; Laurie, V. W.; Kuczkowski, R. L.; Schwendeman, R. H.; Ramsay, D. A.; Lovas, F. J.; Lafferty, W. J.; Maki, A. G. Molecular Structures of Gas-Phase Polyatomic Molecules Determined by Spectroscopic Methods. *J. Phys. Chem. Ref. Data* **1979**, *8* (3), 619.

(103) Suleimenov, O. M.; Seward, T. M. A Spectrophotometric Study of Hydrogen Sulphide Ionisation in Aqueous Solutions to 350°C. *Geochim. Cosmochim. Acta* **1997**, *61* (24), 5187−5198.

(104) Giggenbach, W. Optical Spectra of Highly Alkaline Sulfide Solutions and the Second Dissociation Constant of Hydrogen Sulfide. *Inorg. Chem.* **1971**, *10* (7), 1333−1338.

(105) Bandura, A. V.; Lvov, S. N. The Ionization Constant of Water over Wide Ranges of Temperature and Density. *J. Phys. Chem. Ref. Data* **2006**, *35* (1), 15−30.

(106) Wagner, W.; Pruss, A. International Equations for the Saturation Properties of Ordinary Water Substance. Revised According to the International Temperature Scale of 1990. Addendum to J. Phys. Chem. Ref. Data 16, 893 (1987). *J. Phys. Chem. Ref. Data* **1993**, *22* (3), 783.

(107) Suleimenov, O. M.; Krupp, R. E. Solubility of Hydrogen Sulfide in Pure Water and in NaCl Solutions, from 20 to 320°C and at Saturation Pressures. *Geochim. Cosmochim. Acta* **1994**, *58* (11), 2433−2444.

(108) de Leeuw, N. H.; Cooper, T. G. Surface Simulation Studies of the Hydration of White Rust $Fe(OH)_2$, Goethite α-FeO(OH) and Hematite α-Fe_2O_3. *Geochim. Cosmochim. Acta* **2007**, *71* (7), 1655−1673.

(109) Du, Z.; de Leeuw, N. H. Molecular Dynamics Simulations of Hydration, Dissolution and Nucleation Processes at the α-Quartz (0001) Surface in Liquid Water. *Dalton Trans.* **2006**, No. 22, 2623−2634.

(110) Tafreshi, S. S.; Roldan, A.; de Leeuw, N. H. Hydrazine Network on Cu(111) Surface: A Density Functional Theory Approach. *Surf. Sci.* **2015**, *637−638*, 140−148.

(111) Stoltze, P. Microkinetic Simulation of Catalytic Reactions. *Prog. Surf. Sci.* **2000**, *65* (3−4), 65−150.

(112) Roldán, A.; Novell, G.; Ricart, J. M.; Illas, F. Theoretical Simulation of Temperature Programmed Desorption of Molecular Oxygen on Isolated Au Nanoparticles from Density Functional Calculations and Microkinetics Models. *J. Phys. Chem. C* **2010**, *114* (11), 5101−5106.